Aalborg Universitet

AALBORG UNIVERSITY

Dual Converter Fed Open-End Transformer Topology with Parallel Converters and Integrated Magnetics

Gohil, Ghanshyamsinh Vijaysinh; Bede, Lorand; Teodorescu, Remus; Kerekes, Tamas; Blaabjerg, Frede

Publication date:
2016

Document Version
Early version, also known as pre-print

Link to publication from Aalborg University

Dual Converter Fed Open-End Transformer Topology with Parallel Converters and Integrated Magnetics

Ghanshyamsinh Gohil, *Student Member, IEEE*, Lorand Bede, *Student Member, IEEE*, Remus Teodorescu, *Fellow, IEEE*, Tamas Kerekes, *Senior Member, IEEE*, and Frede Blaabjerg, *Fellow, IEEE*

***Abstract*—A converter system for high power applications, connected to a medium-voltage network using a step-up transformer, is presented in this paper. The converter-side winding of the transformer is configured as an open-end and both the ends of the windings are fed from two different converter groups. Each converter group comprises of two parallel Voltage Source Converters (VSCs), whose carrier signals are interleaved to improve the harmonic quality of the resultant switched output voltage of that converter group. However, an additional inductive component is required to suppress the circulating current that flows between the parallel interleaved VSCs. An integrated inductor is proposed which suppresses the circulating current in both the converter groups. In addition, the functionality of the line filter inductor is also integrated. Flux in various parts of the integrated inductor is analyzed and a design procedure is also described. The volume and the losses of the proposed solution are compared with that of the state-of-art solution. The control of the proposed converter system is also discussed. The analysis has been verified by the simulation and experimental results.**

***Index Terms*—Voltage source converters (VSC), parallel, interleaving, dual converter, open-end transformer, wind power, integrated inductor, magnetic integration, wind energy conversion system**

Nomenclature

$\overrightarrow{\phi}$	Vector representing the flux linkage.
$\overrightarrow{I_c}$	Vector representing the circulating current.
$\overrightarrow{I_r}$	Vector representing the resultant current.
$\overrightarrow{I}$	Vector representing the leg currents of phase x.
$\overrightarrow{V_p}$	Switched output voltage vector.
$\overrightarrow{V_v}$	Voltage vector, representing the potential of the common points of the HSCG and the LSCG.
$\overrightarrow{V}$	Coil voltage vector.
$\boldsymbol{L_c}$	Circulating current inductance matrix.
μ_0	Permeability of the air.
$\overrightarrow{V_H^*}$	Reference voltage space vector for HSCG.
$\overrightarrow{V_L^*}$	Reference voltage space vector for LSCG.
$\phi_{bl_{max}}$	Maximum value of the flux in the bridge legs.
$\phi_{l_{max}}$	Maximum value of the flux in the limbs.

$\phi_{x,k}$	Total flux linking k coil of phase x.
$\phi_{x_{by}}$	Flux in a bottom yoke.
$\phi_{x_{cy}}$	Flux in a common yoke.
$\phi_{x_{k,cmax}}$	Maximum value of the circulating flux component.
$\phi_{x_{k,c}}$	Circulating flux component that links with the kth coil of phase x.
$\phi_{x_{k,f}}$	Fundamental frequency component of the flux that links with the kth coil of phase x.
$\phi_{x_{ty}}$	Flux in a top yoke.
$\phi_{y_{max}}$	Maximum value of the flux in top and bottom yokes.
ψ_H	Reference voltage space vector angle for HSCG.
ψ_L	Reference voltage space vector angle for LSCG.
ψ_{max}	voltage space vector angle for which the circulating flux component achieves its maximum value.
$\Re_l$	Reluctance of a limb.
$\Re_y$	Reluctance of the top, bottom, and common yoke.
$\Re_{bl}$	Reluctance of a bridge leg.
$\Re_{g_1}'$	Equivalent reluctance of an air gap g_1.
$\Re_{g_2}'$	Equivalent reluctance of an air gap g_2.
θ	Displacement power factor angle.
A_g'	Effective cross-section area of the air gap.
A_w	Window area.
A_{c_l}	Cross section area of limb.
A_{cu}	Cross section area of the coil conductor.
B_{m_l}	Permissible value of the flux density in the limb.
B_{m_y}	Permissible value of the flux density in the yoke.
$B_{m_{bl}}$	Permissible value of the flux density in the bridge leg.
C_d	Damping capacitor.
C_f	Shunt capacitive branch of the LCL filter.
I_r	Rated current.
I_x	Resultant line current.
I_{x_H}	Resultant line current of the high-side converter group.
I_{x_k}	Leg current of phase x of the k VSC.
I_{x_L}	Resultant line current of the low-side converter group.
$I_{x_{H,c}}$	Circulating current between the parallel interleaved VSCs of the high-side converter group.
$I_{x_{L,c}}$	Circulating current between the parallel interleaved VSCs of the low-side converter group.
J	Current density.
K_s	Stacking Factor.
K_w	Window utilization factor.
L_c	Circulating current inductance.
L_f	Line filter inductance.

L_g Grid-side inductor of the LCL filter.

l_{g_1} Air gap length between the cell and the bridge leg.

l_{g_2} Length of the air gap in the cell structure.

M Modulation index, defined as the ratio of the peak of the reference signal to the half of the dc-link voltage.

N Number of turns.

R_d Damping resistor.

S VA rating of the converter.

T_s Switching interval.

V_x Resultant phase voltage.

$V_{x'_H o_H}$ Resultant voltage of high-side converter group.

$V_{x'_L o_L}$ Resultant voltage of low-side converter group.

V_{ph} Rated phase voltage.

$V_{x_k o_H}$ Switched output voltage of phase x of kth VSC with respect to the o_H.

$V_{x_k o_L}$ Switched output voltage of phase x of kth VSC with respect to the o_L.

V_{x_s} Resultant switched output voltage of phase x.

$V_{x_{C,f}}$ Voltage across the filter capacitor.

x Subscript, which represents phases a, b, and c.

I. INTRODUCTION

FOR the high power applications, the current can be reduced by using a medium voltage converter. A three-level neutral point diode clamped (3L-NPC) topology is commonly used [1]. However, an extra control efforts are required to balance the dc-link capacitor voltage [2]. Moreover, the semiconductor loss distribution is unequal [3] and this may lead to the de-rating of the Voltage Source Converter (VSC) [4]. On the other hand, the two-level VSC is used extensively in many industrial applications due to its simple power circuitry and proven technology. Therefore, it is highly desirable to realize the medium voltage converter system using the standard two-level VSC.

Many grid-connected applications use transformer between the converter system and the grid for matching the voltage levels. Also in some applications, the grid codes demand galvanic isolation. In such systems, the primary winding can be configured as an open-end winding and can be fed from both the ends using two-level VSCs [5]. The number of levels in the output voltage is same as that of the 3L-NPC and each of the two-level VSC operates with the half of the dc-link voltage than that of the 3L-NPC. However, common-mode (CM) circulating current flows through the closed path if both the VSCs are connected to the common dc-link. But in many applications, isolated dc-links can be readily derived from the source itself and such extra measures for the CM circulating current suppression may not be required. For example, the isolated dc-links can be obtained in

1) PhotoVoltaic (PV) systems by dividing the total number of arrays into two groups to form separate dc-links [5].

2) Wind Energy Conversion System (WECS): isolated dc-links can be obtained using the dual stator-winding generator [6].

Therefore, the analysis presented in this paper is mainly focused on the dual converter fed open-end transformer topology with two separate dc-links.
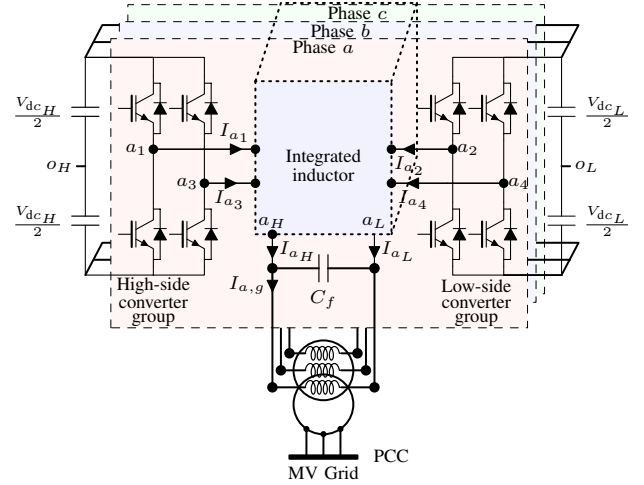

Fig. 1. System configuration of the dual converter fed open-end winding transformer topology with two separate dc-links.

In a dual converter fed open-end transformer topology, each VSC has to process the rated current. In many high power applications, single two-level VSC may not be able to supply the rated current. To overcome this problem, parallel connection of the two-level VSCs in each of the converter groups of the open-end transformer topology is proposed, as shown in Fig. 1. In this way, both the voltage and the current handling capability of the converter can be increased.

Another issue in the high power converter is the limited switching frequency capability of the semiconductor devices [7]. Therefore, large filter components are generally employed in order to comply with the stringent power quality requirements imposed by the utility [8]. This leads to the increased cost, size and losses. The size of the filter components can be reduced by improving the harmonic quality of the output voltage of each of the converter groups by interleaving the carrier signals of the parallel connected VSCs [9], [10]. However, circulating current is generated between the parallel VSCs due to hardware and control asymmetries and carrier interleaving further aggravates this problem. This unwanted circulating current increases the stress on the semiconductor switches, causes additional losses and it should be suppressed.

The circulating current between the parallel VSCs can be suppressed by providing magnetic coupling between the parallel interleaved legs of the corresponding phases [11], [12]. Therefore, in addition to a line filter inductor, a circulating current filter inductor is also required. The size of these inductors can be significantly reduced by integrating them into a single magnetic component [13]–[16]. A magnetic integration of both the circulating filter inductor and the line filter inductor of both the converter groups is presented in this paper and the design methodology is also described. The paper is organized as follows: the system is described in Section II. The integrated inductor is analyzed in Section III. The design of the integrated inductor is illustrated in Section IV. The control scheme and the comparative evaluation is presented in Section V. Section VI summarizes the simulation and hardware results.

TABLE I
PHASE SHIFT BETWEEN THE CARRIER SIGNALS

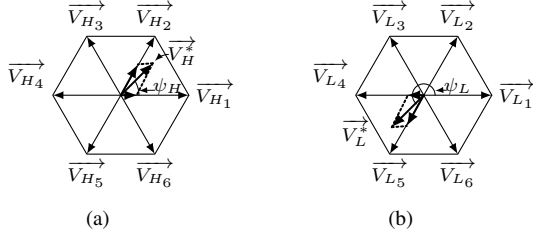| Converter	VSC$_1$	VSC$_2$	VSC$_3$	VSC$_4$
Phase shift	0°	90°	180°	270°

(a)

Fig. 2. Reference voltage space vector and its formation by the geometrical summation. (a) Reference voltage space vector for the VSCs of the high-side converter group, (b) Reference voltage space vector for the VSCs of the low-side converter group. The voltage space vector angle of the low-side converter group $\psi_L = 180° + \psi_H$.
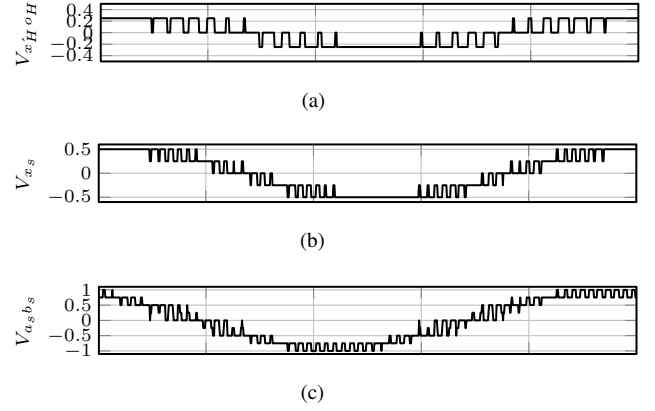

Fig. 3. Switched voltages with the modulation index $M = 1$ and the switching frequency of 750 Hz, These voltages are normalized to $(V_{dc_H} + V_{dc_L})/2$. (a) Resultant switched output voltage of the high-side converter group, (b) Resultant switched output voltage, (c) Resultant line to line voltage $V_{a_s b_s}$.

II. SYSTEM DESCRIPTION

A dual converter fed open-end winding transformer topology with two separate dc-links is shown in Fig. 1. Four two-level three phase VSCs are used. Out of these four VSCs, VSC$_1$ and VSC$_3$ are connected in parallel and share the same dc-link. The carrier signals of these two parallel two-level VSCs are interleaved. As a result, three-level resultant voltage waveforms can be achieved [10], [13]. Therefore, the parallel connection of the VSC$_1$ and the VSC$_3$ can be treated as a single three-level converter and referred to as a High-Side Converter Group (HSCG). Similarly, the parallel connection of the VSC$_2$ and VSC$_4$ forms another converter group, which is referred to as a Low-Side Converter Group (LSCG). The low-voltage side of the transformer winding is configured as an open-end and fed from both the ends using the HSCG and the LSCG.

The carrier signals of the parallel connected VSCs are symmetrical interleaved and the phase shift between the carrier signals is given in Table I. Due to the carrier interleaving, the switched output voltages of the respective phases of both the VSCs are also phase shifted and yield three-level resultant voltage waveform. However, the instantaneous potential difference appears across the close path when the carrier signals are interleaved. This potential difference could drive large circulating current between the parallel VSCs due to the use of the common dc-link. This leads to the increase in the stress and the losses of the semiconductor devices and the passive components. Therefore, it is important to suppress the circulating current to some acceptable value to realize the full potential of the carrier interleaving.

A. Modulation

The reference voltage space vectors of both the HSCG and the LSCG have the same magnitude. However, the respective voltage space vector angles (ψ_H and ψ_L) have a phase difference of $180°$, as shown in Fig. 2. VSCs in both the converter groups are modulated using the $60°$ clamp

discontinuous PWM (DPWM1) scheme [17]. As most of the grid-connected renewable energy systems operate with the power factor close to one, the switching losses can be reduced upto 50% compared to that of the continuous space vector modulation [18] using the DPWM1.

B. Harmonic Quality Assessment

For the parallel interleaved VSCs, the resultant switch output voltage of a given phase is the average of the individual switched output voltages of the parallel interleaved legs of that phase and for the HSCG, it is given as

$$V_{x'_H o_H} = \frac{V_{x_1 o_H} + V_{x_3 o_H}}{2} \qquad (1)$$

Similarly, the resultant output voltage of the LSCG is given as

$$V_{x'_L o_L} = \frac{V_{x_2 o_L} + V_{x_4 o_L}}{2} \qquad (2)$$

The simulated resultant voltage waveform of the HSCG over a fundamental period is shown in Fig. 3(a), which exhibits three-level voltage waveforms. The closed form theoretical harmonic solution for resultant voltage for asymmetrical regular sampled DPWM1 is derived in [10] and it is used to obtain the harmonic spectra of the resultant voltage of both the converter groups. As a result of the interleaved carrier signals, the magnitude of odd multiple of the carrier frequency harmonic and their side band is considerably reduced in the $V_{x'_H o_H}$.

The resultant switched output voltage V_{x_s} is the difference of the resultant switched output voltages of the HSCG and the LSCG and it is given as

$$V_{x_s} = V_{x'_H o_H} - V_{x'_L o_L} \qquad (3)$$

The simulated waveform of the resultant switched output voltage of phase a (V_{a_s}) over a fundamental period is shown in Fig. 3(b). The V_{a_s} has a multi-level voltage waveform and the major harmonic component appears at the $4th$ carrier harmonic frequency component. The resultant switched output
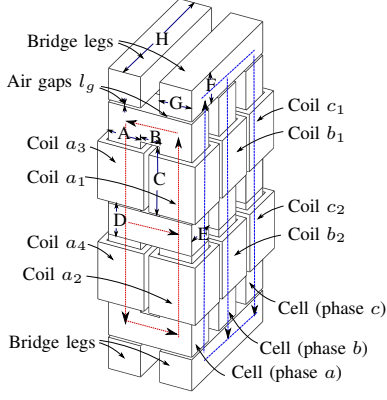
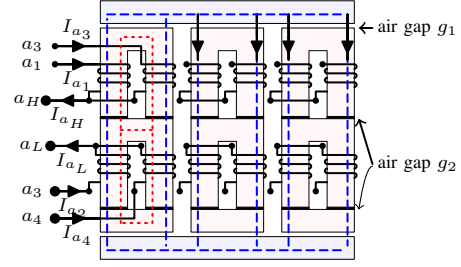Fig. 4. Physical layout of the proposed integrated inductor.

Fig. 5. Magnetic core structure of the integrated inductor. The flux paths are illustrated when the coils of phase a are excited.

Fig. 6. Simplified reluctance model of the integrated inductor.

voltage has significant triplen baseband harmonic component. However, due to the three-wire system and isolated dc-links, these voltage components do not generate any triplen harmonic frequency current. The resultant line-to-line voltage, which determines the quality of the output current is also shown in Fig. 3(c).

III. INTEGRATED INDUCTOR

The switched output voltage exhibits five-level voltage waveform as discussed in section II. However, the circulating current flows between the parallel interleaved VSCs of the HSCG (as well as between the VSCs of the LSCG). The integrated inductor suppresses these circulating currents. Moreover, the integrated inductor also combines the functionalities of the converter-side inductor L_f of the LCL filter (which is required to achieve desired harmonic quality of the injected line current). The magnetic structure and the analysis of the integrated inductor is presented in this section.

A. Magnetic Structure of Integrated Inductor

The physical layout of the proposed integrated inductor is shown in Fig. 4. The magnetic core is composed of three identical cells for each of the phases of the three-phase system. Each cell has two limbs and these limbs are magnetically coupled to each other using the top, the common, and the bottom yokes. This arrangement forms two windows in each of the cells. Top window provides the space to receive the coils corresponding to the HSCG (coils x_1 and x_3). Similarly, the coils of the LSCG are also placed around the limbs and accommodated in the bottom window area of the cell, as shown in Fig. 4. The cells of all the three phases are magnetically coupled to each other using the bridge legs. Necessary air gaps (g_1 as shown in Fig. 5) are introduced between the cells and the bridge legs in order to provide energy storage to achieve the desired value of the converter-side inductor L_f. Similarly small air gaps (g_2 as shown in Fig. 5) are also provided in the cell structure to obtain the desired value of the circulating current inductance.

The starting terminals of both the coils of phase x, housed in the top window, are connected to the output terminals of phase x of the VSCs of the HSCG (x_1 and x_3), whereas the ending terminals are connected together to form the common connection point x_H, as shown in Fig. 5. Similarly, the output
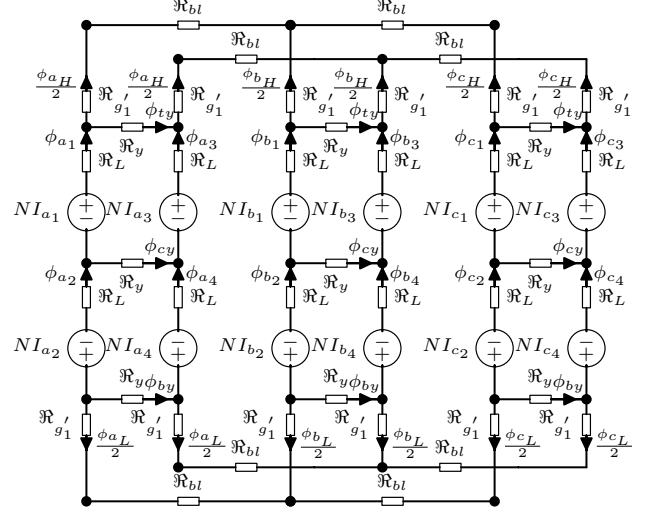
terminals of the phase x of the VSCs of the LSCG (x_2 and x_4) are connected to the starting terminals of the coils housed in the bottom window and ending terminals are connected to the common point x_L. Both of the coils of the particular converter group are wound in the same direction. However, the direction of the coils of the HSCG cell is opposite to the direction of the coils of the LSCG cell, as shown in Fig. 5.

B. Flux Linking with the Coils

The simplified reluctance model of the proposed inductor is shown in Fig. 6. The permeability of the magnetic material is assumed to be constant and the effect of the leakage flux is neglected. The analysis is presented for one of the phases. By solving the reluctance model, the flux linking with each of the coils is given as

$$\phi_{x_1} = \frac{L_1}{N}(I_{x_1} + I_{x_3}) + \frac{L_2}{2N}(I_{x_1} - I_{x_3}) - \frac{L_3}{2N}(I_{x_2} - I_{x_4}) \quad (4)$$

$$\phi_{x_2} = -\frac{L_1}{N}(I_{x_2} + I_{x_4}) - \frac{L_2}{2N}(I_{x_2} - I_{x_4}) + \frac{L_3}{2N}(I_{x_1} - I_{x_3}) \quad (5)$$

$$\phi_{x_3} = \frac{L_1}{N}(I_{x_1} + I_{x_3}) - \frac{L_2}{2N}(I_{x_1} - I_{x_3}) + \frac{L_3}{2N}(I_{x_2} - I_{x_4}) \quad (6)$$

$$\phi_{x_4} = -\frac{L_1}{N}(I_{x_2} + I_{x_4}) + \frac{L_2}{2N}(I_{x_2} - I_{x_4}) - \frac{L_3}{2N}(I_{x_1} - I_{x_3}) \quad (7)$$

where

$$L_1 = \frac{N^2}{2\Re_L + 2\Re_{bl} + 2\Re_{g_1'}} \tag{8}$$

$$L_2 = \frac{4N^2(\Re_L + \Re_y)}{(2\Re_L + \Re_y)(2\Re_L + 3\Re_y)} \tag{9}$$

$$L_3 = \frac{2N^2\Re_y}{(2\Re_L + \Re_y)(2\Re_L + 3\Re_y)} \tag{10}$$

R_L is the sum of the reluctance of the limb and the reluctance of the air gap g_2 and it is given as $R_L = R_l + \Re_{g_2'}$.

The flux in the top and the bottom yokes of the cell are given as

$$\phi_{x_{ty}} = \frac{L_2}{2N}(I_{x_1} - I_{x_3}) - \frac{L_3}{2N}(I_{x_2} - I_{x_4}) \tag{11}$$

$$\phi_{x_{by}} = \frac{L_2}{2N}(I_{x_2} - I_{x_4}) - \frac{L_3}{2N}(I_{x_1} - I_{x_3}) \tag{12}$$

and flux in the common yoke is:

$$\phi_{x_{cy}} = \frac{N}{2\Re_l + 3\Re_y}(-I_{x_1} - I_{x_2} + I_{x_3} + I_{x_4}) \tag{13}$$

From the fluxes, the voltage across each of the coils can be obtained as

$$\overrightarrow{V} = \overrightarrow{V_p} - \overrightarrow{V_v} = N\frac{d}{dt}\overrightarrow{\phi} \tag{14}$$

where $\overrightarrow{V}$, $\overrightarrow{V_p}$ and $\overrightarrow{V_v}$ are the voltage vectors and they are represented as

$$\overrightarrow{V} = \begin{bmatrix} V_{x_1 x_H} & V_{x_2 x_L} & V_{x_3 x_H} & V_{x_4 x_L} \end{bmatrix}^T \tag{15}$$

$$\overrightarrow{V_p} = \begin{bmatrix} V_{x_1 o_H} & V_{x_2 o_L} & V_{x_3 o_H} & V_{x_4 o_L} \end{bmatrix}^T \tag{16}$$

$$\overrightarrow{V_v} = \begin{bmatrix} V_{x_H o_H} & V_{x_L o_L} & V_{x_H o_H} & V_{x_L o_L} \end{bmatrix}^T \tag{17}$$

$$\overrightarrow{\phi} = \begin{bmatrix} \phi_{x_1} & \phi_{x_2} & \phi_{x_3} & \phi_{x_4} \end{bmatrix}^T \tag{18}$$

C. Line Filter Inductor and Circulating Current Inductor

The leg currents I_{x_k} has two components:

1) Resultant line current component (comprises of fundamental frequency component and small ripple current component).
2) Circulating current component.

Assuming equal current sharing between the parallel connected VSCs, the leg current vector can be decomposed as

$$\overrightarrow{I} = \overrightarrow{I_r} + \overrightarrow{I_c} \tag{19}$$

where

$$\overrightarrow{I} = \begin{bmatrix} I_{x_1} & I_{x_2} & I_{x_3} & I_{x_4} \end{bmatrix}^T \tag{20}$$

$$\overrightarrow{I_r} = \begin{bmatrix} \frac{I_{x_H}}{2} & \frac{I_{x_L}}{2} & \frac{I_{x_H}}{2} & \frac{I_{x_L}}{2} \end{bmatrix}^T \tag{21}$$

$$\overrightarrow{I_c} = \begin{bmatrix} I_{x_{H,c}} & I_{x_{L,c}} & -I_{x_{H,c}} & -I_{x_{L,c}} \end{bmatrix}^T \tag{22}$$

where the resultant current components are

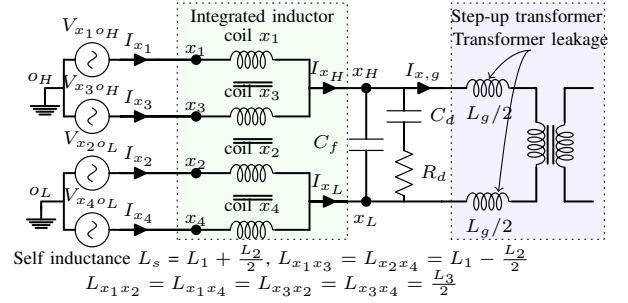$$I_{x_H} = I_{x_1} + I_{x_3} , \; I_{x_L} = I_{x_2} + I_{x_4} \tag{23}$$

Fig. 7. Electrical equivalent circuit of the integrated inductor.

and circulating current components are given as

$$I_{x_{H,c}} = \frac{I_{x_1} - I_{x_3}}{2} \text{ and } I_{x_{L,c}} = \frac{I_{x_2} - I_{x_4}}{2} \tag{24}$$

Using (14), the voltages across the coil x_1 and x_3 are obtained and substituting the leg currents in these equation yield

$$V_{x_1 o_H} - V_{x_H o_H} = L_1\frac{dI_{x_H}}{dt} + L_2\frac{dI_{x_{H,c}}}{dt} - L_3\frac{dI_{x_{L,c}}}{dt} \tag{25}$$

$$V_{x_3 o_H} - V_{x_H o_H} = L_1\frac{dI_{x_H}}{dt} - L_2\frac{dI_{x_{H,c}}}{dt} + L_3\frac{dI_{x_{L,c}}}{dt} \tag{26}$$

Averaging the voltages across the coils of the HSCG (25) and (26) yields

$$V_{x_H' o_H} - V_{x_H o_H} = L_1\frac{dI_{x_H}}{dt} \tag{27}$$

where $V_{x_H' o_H}$ is the average value of the switched output voltages of the HSCG, as given in (1). Similarly, the voltages across the coils x_2 and x_4 are given as

$$V_{x_2 o_L} - V_{x_L o_L} = -L_1\frac{dI_{x_L}}{dt} - L_2\frac{dI_{x_{L,c}}}{dt} + L_3\frac{dI_{x_{H,c}}}{dt} \tag{28}$$

$$V_{x_4 o_L} - V_{x_L o_L} = -L_1\frac{dI_{x_L}}{dt} + L_2\frac{dI_{x_{L,c}}}{dt} - L_3\frac{dI_{x_{H,c}}}{dt} \tag{29}$$

and averaging the voltage across the coils of the LSCG gives

$$V_{x_L' o_L} - V_{x_L o_L} = L_1\frac{dI_{x_L}}{dt} \tag{30}$$

where $V_{x_L' o_L}$ is the average value of the switched output voltage of the LSCG, as given by (2).

The electrical equivalent circuit of the integrated inductor is derived and it is shown in Fig. 7. For the open-end transformer topology, the resultant line current $I_x = I_{x_H} = -I_{x_L}$. Substituting this in (27) and (30) give

$$V_{x_s} - V_{x_{C,f}} = 2L_1\frac{dI_x}{dt} \tag{31}$$

where V_{x_s} is the resultant switched voltage and and $V_{x_{C,f}}$ is the voltage across the line filter capacitor C_f and given as

$$V_{x_s} = \left(\frac{V_{x_1 o_H} + V_{x_3 o_H}}{2}\right) - \left(\frac{V_{x_2 o_L} + V_{x_4 o_L}}{2}\right) \tag{32}$$

and

$$V_{x_{C,f}} = V_{x_H o_H} - V_{x_L o_L} \tag{33}$$

Since two separate dc-links are employed, the common mode circulating current between the HSCG and the LSCG is zero and I_{x_H} and I_{x_L} only have the differential current

components. Therefore, using (31), the line filter inductance L_f is given as

$$L_f = \frac{2N^2}{2\Re_l + 2\Re_{bl} + 2\Re_{g_1'} + 2\Re_{g_2'}} = \mu_0 N^2 \Big(\frac{A_{g_1'}}{l_{g_1}} + \frac{A_{g_2'}}{l_{g_2}}\Big) \quad (34)$$

where $A_{g_1'}$ and $A_{g_2'}$ are the effective cross-section area of an air gaps g_1 and g_2, respectively and it can be obtained by evaluating the cross-section area of the air gap after adding length of the air gap to each dimension in the cross-section.

For the parallel interleaved VSCs, the switched output voltages of the parallel interleaved legs are phase shifted and the difference of these voltages drives the circulating current. Using (25) and (26), the difference of the switched output voltages of the parallel VSCs of the HSCG is given as

$$V_{x_1 o_H} - V_{x_3 o_H} = 2L_2 \frac{dI_{x_{H,c}}}{dt} - 2L_3 \frac{dI_{x_{L,c}}}{dt} \quad (35)$$

similarly, subtracting (29) from (28) yields

$$V_{x_2 o_L} - V_{x_4 o_L} = 2L_3 \frac{dI_{x_{H,c}}}{dt} - 2L_2 \frac{dI_{x_{L,c}}}{dt} \quad (36)$$

Using (35) and (36), the circulating currents are described as

$$\begin{bmatrix} V_{x_1 o_H} - V_{x_3 o_H} \\ V_{x_2 o_L} - V_{x_4 o_L} \end{bmatrix} = \boldsymbol{L_c} \frac{d}{dt} \begin{bmatrix} I_{x_{H,c}} \\ I_{x_{L,c}} \end{bmatrix} \quad (37)$$

where $\boldsymbol{L_c}$ is the circulating current inductance matrix and given as

$$\boldsymbol{L_c} = \begin{bmatrix} 2L_2 & -2L_3 \\ -2L_3 & 2L_2 \end{bmatrix} \quad (38)$$

The value of L_c should be chosen to limit the circulating current to some acceptable limits.

IV. DESIGN METHODOLOGY

The design equations for the integrated inductor are derived in this section. The design methodology is also illustrated by carrying out the design of the integrated inductor for a 12 MW, 3.3 kV Wind Energy Conversion System (WECS).

A. Design Equations

The flux linking with each of the coils can be decomposed into three categories:

1) Fundamental frequency flux component.
2) Ripple component of the flux with dominant component at $4th$ carrier frequency harmonic.
3) Circulating flux with dominant component at $1st$ carrier frequency harmonic.

The ripple component of the flux is very small compared to the fundamental frequency component and the circulating flux component. Therefore, the effect of the ripple component is neglected in the design.

1) Fundamental Frequency Flux Component $\phi_{x_{k,f}}$: Using (4), the fundamental component of the flux linking with the coil is given as

$$\phi_{a_{k,f}}(t) = \frac{L_f S}{3\sqrt{2} N V_{ph}} \cos(\psi - \theta) \quad (39)$$

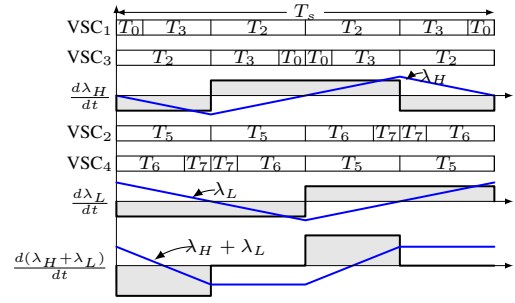$\phi_{a_{k,f}}$ attains its maximum value for the space vector angle $\psi = \theta$.

Fig. 8. The switching sequences and switched output voltage difference of the HSCG and the LSCG for phase a for $M = 1$ and $\psi_H = 84.7°$.

2) Circulating Flux Component $\phi_{x_{k,c}}$: From (4) and (6), the circulating flux components that links with the coils of the HSCG are obtained as

$$\phi_{a_{1,c}}(t) = -\phi_{a_{3,c}}(t) = \frac{L_2}{N} I_{a_{H,c}} - \frac{L_3}{N} I_{a_{L,c}} \quad (40)$$

By obtaining the values of the $I_{a_{H,c}}$ and $I_{a_{L,c}}$ from (37) and substituting in (40) yields

$$\phi_{a_{1,c}}(t) = -\phi_{a_{3,c}}(t) = \frac{\lambda_H(t)}{2N} \quad (41)$$

where

$$\lambda_H(t) = \int (V_{a_1 o_H} - V_{a_3 o_H}) dt \quad (42)$$

Similarly, the circulating flux component that links with the coils of the LSCG are obtained as

$$\phi_{a_{2,c}}(t) = \frac{1}{2N} \int (V_{a_2 o_L} - V_{a_4 o_L}) dt = \frac{\lambda_L(t)}{2N} \quad (43)$$

The analysis of the variation of the $\lambda_H(t)$ with the modulation index M and the space vector angle ψ is presented in [19], [20]. The peak value of the $\lambda_H(t)$ is different in every sampling interval due to the change in the dwell times of the voltage vector. Let the maximum value out of these peak values is $\lambda_{H_{max}}$ and it is given as

$$\lambda_{H_{max}} = \begin{cases} \frac{\sqrt{3}M}{4} V_{dc_H} T_s, & 0 \le M < 1/\sqrt{3} \\ \frac{1}{4} V_{dc_H} T_s, & 1/\sqrt{3} \le M < 2/\sqrt{3} \end{cases} \quad (44)$$

For the grid connected applications, the modulation index M varies in a small range close to one. Therefore, the maximum value of the circulating flux component is given as

$$\phi_{a_{1,c_{max}}} = \frac{V_{dc_H} T_s}{8N} \quad (45)$$

The $\phi_{a_{1,c}}(t)$ achieves $\phi_{a_{1,c_{max}}}$ value at the space vector angle ψ_{max}, as shown in Fig. 8 and ψ_{max} is given as

$$\psi_{max} = 120° - \arcsin(\frac{1}{\sqrt{3}M}) \quad (46)$$

3) Maximum Flux Value in the Bridge Legs: The common component of the fluxes that links with coils x_1 and x_3 pass through the bridge legs and the maximum value of this flux component is given as

$$\phi_{bl_{max}} = \frac{L_f S}{3\sqrt{2} N V_{ph}} \quad (47)$$

TABLE II
VALUES OF THE FLUX IN THE LIMB FOR DIFFERENT VOLTAGE SPACE
VECTOR ANGLES

Value	Conditions
$N\phi_{a_l}(t)\mid_{\psi=0°} = \dfrac{L_f S}{3\sqrt{2}V_{ph}}$	$\theta = 0°$
$N\phi_{a_l}(t)\mid_{\psi=30°} = \dfrac{0.978L_f S}{3\sqrt{2}V_{ph}} + \dfrac{0.354V_{dc_H}T_s}{8}$	$\theta = 18°,\ M = 0.95$
$N\phi_{a_l}(t)\mid_{\psi=82.5°} = \dfrac{0.429L_f S}{3\sqrt{2}V_{ph}} + \dfrac{V_{dc_H}T_s}{8}$	$\theta = 18°,\ M = 0.95$

TABLE III
SYSTEM PARAMETERS FOR SIMULATION AND EXPERIMENTAL STUDY

Parameters	Simulation study	Experiment
Power	13.2 MVA (12 MW)	11 kVA (10 kW)
Switching frequency	750 Hz	750 Hz
AC voltage (line-to-line)	3300 V	400 V
$V_{dc_H} = V_{dc_L}$	2900 V	350 V
Base impedance	0.825 Ω	14.54 Ω
Base inductance	2.6 mH	46.3 mH
Base capacitance	3.9 mF	0.218 mF
L_f	370 μH (0.14 pu)	6.1 mH (0.135 pu)
L_g	290 μH (0.11 pu)	5 mH (0.11 pu)
$C_f = C_d$	193 μF (0.05 pu)	11 μF (0.05 pu)
L_c	2.2 mH (0.85 pu)	39 mH (0.85 pu)

4) Maximum Flux Value in the Top and the Bottom Yokes:
The circulating component of the flux is confined in the cell. Therefore, the maximum value of the flux in the top and the bottom yokes $\phi_{y_{max}}$ is

$$\phi_{y_{max}} = \frac{V_{dc_H}T_s}{8N} \quad (48)$$

5) Maximum Flux Value in the Common Yoke: Using (13), the flux in the common yoke is obtained as

$$\phi_{cy}(t) = \frac{-2N}{2\Re_l + 3\Re_y}(I_{a_{H,c}} + I_{a_{L,c}}) \quad (49)$$

Substituting the values of $I_{a_{H,c}}$ and $I_{a_{L,c}}$ in (49) yields

$$\phi_{cy}(t) = \frac{1}{2N}[\lambda_H(t) + \lambda_L(t)] \quad (50)$$

The difference of the switched output voltages of the HSCG and the LSCG are shown in Fig. 8. The voltage level of the $d(\lambda_H(t) + \lambda_L(t))/dt$ is $V_{dc_H} + V_{dc_L}$, which is twice as that of the $d\lambda_H(t)/dt$ and $d\lambda_L(t)/dt$. However, the duration for which this voltage appears is half than that of the $d\lambda_H(t)/dt$ and $d\lambda_L(t)/dt$. The maximum value of the $\phi_{cy}(t)$ is given as

$$\phi_{cy_{max}} = \frac{(V_{dc_H} + V_{dc_L})T_s}{16N} \quad (51)$$

Assuming $V_{dc_H} = V_{dc_L}$, the value of the $\phi_{cy_{max}} = \phi_{y_{max}}$. Therefore, despite the common yoke carrying the sum of the circulating fluxes of the HSCG and the LSCG, the required cross-section area of the common yoke is the same as that of the top and the bottom yokes. This also leads to the volume reduction of the integrated inductor.

6) Maximum Flux Value in the Limb: The flux in the limb is given as

$$\phi_{a_l}(t) = \phi_{a_{1,f}}(t) + \phi_{a_{1,c}}(t) \quad (52)$$

As it is evident from (39), the space voltage vector angle at which the $\phi_{a_{1,f}}$ attains the maximum value depends on the displacement power factor angle. Whereas, the space vector angle at which the $\phi_{a_{1,c}}$ attains the maximum value depends on the modulation index M, as given in (46). Therefore, in order to obtain the worst case value of the flux $\phi_{l_{max}}$, the operating range of the θ and M should be known. For the WECS application, the converter should be able to supply the current with the displacement power factor within a range of 0.95 lagging to 0.95 leading [8]. Therefore, the displacement power factor angle varies from $-18°$ to $18°$ ($-18° \leq \theta \leq 18°$). The modulation index in grid connected application varies in a small range in vicinity to one and therefore M is assumed to be vary between 0.95 to 1.1 ($0.95 \leq M \leq 1.1$). The flux

linkage in the limb for different space voltage vector angels for specific operating conditions are given in Table II. The maximum value of the flux in the limb $\phi_{l_{max}}$ is maximum out of the flux values given in Table II.

B. Design Example

The integrated inductor is designed for the 13.2 MVA, 3.3 kV WECS. A small scale prototype has been also designed and built. The system parameters of both the systems are specified in Table III. The parameters of the line filter are obtained using the procedure outlined in [10], [21], [22]. The functionalities of the converter-side inductor L_f and the circulating current inductor are integrated in the designed inductor.

The line filter inductor for the high power systems generally requires large air gap and it is often realized by having several discrete air gaps. However, in the case of the proposed integrated inductor, the length of the air gap in the cell structure (l_{g_2}) is limited by the required value of the circulating current inductance as given in (9), (10), and (38). The design example of the high power system is considered to demonstrate how to address this issue and two possible approaches are presented.

1) Integrated Inductor Using Discrete Bridge Blocks: In this approach, several discrete core blocks with an air gap in between them are inserted between the cell and the bridge legs to realize several discrete air gaps. The first iteration of the design parameters are obtained using the steps illustrated below and then the Finite Element Analysis (FEA) is carried out to fine tune the design parameters.

The maximum value of the flux density in the limb is obtained as

$$B_{l_{max}} = \frac{1}{NA_{c_l}}\left(\frac{0.429L_f S}{3\sqrt{2}V_{ph}} + \frac{V_{dc_H}T_s}{8}\right) \quad (53)$$

Each of the windows should be able to carry two coils with half of the rated current flowing through it. Therefore,

$$N = \frac{K_w A_w J}{I_r} \quad (54)$$

Using (53) and (54), the product of the cross section area of the limb and the window area is obtained as

$$A_{c_l}A_w = \frac{I_r}{B_{m_l}JK_w}\left(\frac{0.429L_f S}{3\sqrt{2}V_{ph}} + \frac{V_{dc_H}T_s}{8}\right) \quad (55)$$

TABLE IV
PARAMETERS OF THE DESIGNED INTEGRATED INDUCTOR. SEE FIG. 4
FOR DEFINITIONS. ALL PARAMETERS ARE GIVEN IN MM.

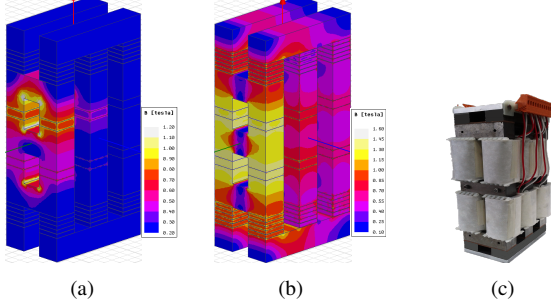| System	A,B,E,F,G	C	D	H	N	A_{cu} (mm^2)
12 MW	205	300	180	1025	14	400
10 kW	25	75	25	25	104	2.62

(a)　　　　　(b)　　　　　(c)

Fig. 9. The flux density distribution in the magnetic core. (a) Phase shifted components of switched output voltage of the carrier frequency harmonics are applied across the coils (space vector angle is $240°$. Therefore, phase c is clamped to the dc bus, so the coils of the cells of only phase a and phase b are excited), (b) Coils are excited with the common component of the current ($I_{a_k} = 1600$ A, $I_{b_k} = I_{c_k}$ =-800A), (c) Photograph of the implemented inductor for a 11 kVA prototype.

Suitable core to match the area product requirement should be selected. Once the value of A_{c_l} is known, the number of turns in each coil is obtained by using (53) and it is given as

$$N = \frac{1}{B_{m_l}A_{c_l}}\left(\frac{0.429L_fS}{3\sqrt{2}V_{ph}} + \frac{V_{dc_H}T_s}{8}\right) \quad (56)$$

where $A_{c_l} = K_s \times A \times E$ for the geometrical parameters shown in Fig. 4. Only the circulating flux component flows through the yokes and the cross-section area of the yokes can be obtained as

$$A_{c_y} = \frac{V_{dc_H}T_s}{8NB_{m_y}} \quad (57)$$

The cross section area of the bridge leg can be obtained from (47) and it is given as

$$A_{c_{bl}} = \frac{L_fS}{3\sqrt{2}NB_{m_{bl}}V_{ph}} \quad (58)$$

and the $A_{c_{bl}} = K_s \times G \times F$. The inductance offer to the circulating current is given as

$$L_c \approx 2L_2 = \frac{2N^2}{\Re_{g_2'}} = \frac{2\mu_0 N^2 A_{g_2'}}{l_{g_2}} \quad (59)$$

Using (59), the value of the l_{g_2} is obtained. Once l_{g_2} is know, the value of l_{g_1} is obtained using (34).

The design parameters obtained using the outlined procedure are fine tuned using the FEA and they are specified in Table IV. Two air gaps having 3 mm length each is inserted in the cell structure and six discrete air gaps of 2.6 mm length have been inserted between the cell and the bridge legs. The window utilization factor K_w is taken to be 0.3 and the current density is considered to be J =3 A/mm^2. The flux density distribution is shown in Fig. 9(a) and Fig. 9(b). The inductance values are obtained by using the FEA and the L_f and L_c are calculated to be 395μH and 2.2 mH, respectively.
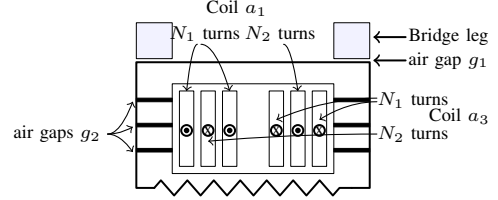

Fig. 10. Integrated inductor with split winding arrangement.

TABLE V
DESIGN EQUATIONS FOR INTEGRATED INDUCTOR WITH SPLIT
WINDINGS

Parameter	Value
$\phi_{a_k,f_{max}} = \phi_{bl_{max}}$	$\frac{L_fS}{3\sqrt{2}(N_1-N_2)V_{ph}}$
$\phi_{a_1,c_{max}} = \phi_{y_{max}}$	$\frac{V_{dc_H}T_s}{8(N_1+N_2)}$
$\phi_{cy_{max}}$	$\frac{(V_{dc_H}+V_{dc_L})T_s}{16(N_1+N_2)}$
L_f	$\mu_0(N_1-N_2)^2\left(\frac{A_{g_1'}}{l_{g_1}} + \frac{A_{g_2'}}{l_{g_2}}\right)$
L_c	$\frac{2}{l_{g_2}}\mu_0(N_1+N_2)^2 A_{g_2'}$

2) Integrated Inductor Using Split Windings: In the above mentioned approach, several discrete air gaps are realized by using the bridge blocks as shown in Fig. 9(a) and Fig. 9(b). The requirement of the additional bridge blocks can be avoided by introducing discrete air gaps in the cell structure (which increases the value of the l_{g_2}). However, this leads to the increase in the reluctance of the limb $\Re_L$, which in turn result in the low value of the circulating current inductance L_c. For the given l_{g_2}, high value of L_c can be achieved by increasing the number of turns. However, increasing the number of turns also affects the value of the L_f and demands larger value of the l_{g_1}, as it is evident from (34). The values of both the L_f and L_c depend on the number of turns and may sometime cause design bottleneck. This can be addressed by using the split coils, as shown in Fig. 10.

The coil arrangement of the HSCG of phase a is shown in Fig. 10 for the illustration. The number of turns in coil a_1 is split into two parts. The first part with N_1 number of the turns is wound around the limb a_1 with the coil direction shown in Fig. 10, whereas other part with N_2 turns wound around limb a_3 in the opposite direction of that of the first part. The same arrangement has been done for the coil a_3 as well. In this arrangement, the common component of the flux produced by N_1 turns of the coil a_1 is in opposite to the common component of the flux produce by the N_2 turns of the coil a_3. On the other hand, the circulating flux components produced by the N_1 turns of the coil a_1 and N_2 turns of the coil a_3 are in the same direction. As result, the desired value of the L_f and L_c can be obtained by choosing proper values of the N_1 and N_2. The relevant design equations are given in Table V.

V. CONTROL SCHEME AND PERFORMANCE EVALUATION

A. Control Scheme

The control scheme is designed to inject the desired active and reactive current, as shown in Fig. 11. The parameter mis-
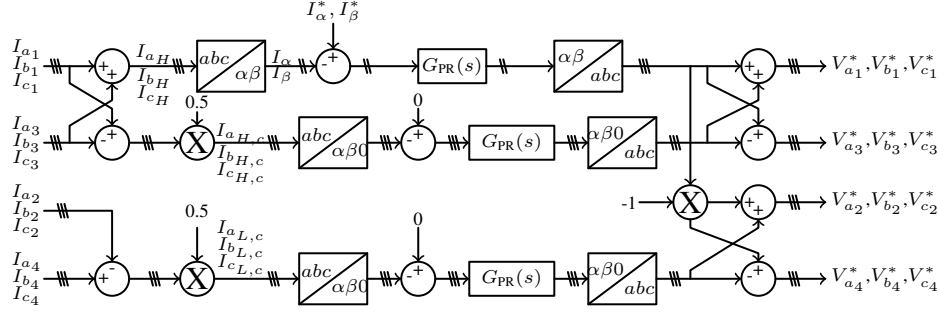
Fig. 11. Control scheme.

match between the parallel converter may cause fundamental frequency component to be present in the circulating current, which may cause the saturation of the integrated inductor. Therefore, the control scheme is also designed to maintain equal current sharing between the parallel VSCs.

1) Active and Reactive Current Control: The active and the reactive currents are controlled by controlling the resultant output current of the HSCG I_{a_H}. As $I_{a_H} = -I_{a_L}$, the resultant current of the LSCG is also indirectly controlled. The control variables are transformed into a $\alpha\beta$ frame and controlled using the Proportional-Resonant (PR) controller. The PR controller is represented as $G_{PR}(s)$ and it is given as

$$G_{PR}(s) = K_p + k_i \frac{s}{s^2 + \omega_0^2} \tag{60}$$

where ω_0 is the angular speed of the grid voltage and k_p and k_i are the proportional and the integral gain of the PR controller. The control and PWM delay is represented by the first order approximation of the $G_d(s)$, where $G_d(s) = e^{-\frac{sT_s}{4}}$. From Fig. 7 and using (31), (32), and (33), the filter transfer $G_f(s) = I_x(s)/V_x(s)$ is derived as

$$G_f(s) = \frac{1}{sL_f} \frac{s^3 + s^2 \frac{C_f + C_d}{C_f C_d R_d} + s \frac{1}{L_g C_f} + \frac{1}{L_g C_f C_d R_d}}{s^3 + s^2 \frac{C_f + C_d}{C_f C_d R_d} + s \frac{L_f + L_g}{L_f L_g C_f} + \frac{L_f + L_g}{L_f L_g C_f C_d R_d}} \tag{61}$$

The parameters of the designed filter are given in Table III. The continuous transfer functions are discretized and the current controller parameters are calculated in the discrete time domain using the root locus theory. The parameters of the PR controller of the active and reactive current controller are $K_p = 3.1 \ \Omega$ and $K_i = 605 \ \Omega/s$.

2) Circulating Current Control: The circulating current between the parallel VSCs in both the HSCG and the LSCG is controlled by modifying the reference voltage generated by the active and reactive current control loop. The circulating current is obtained from the leg currents. As the leg currents are sampled at the top and the bottom of the carrier signals, the switching frequency ripple component is filtered out. The fundamental frequency component of the circulating current is then controlled to be zero using the Proportional-Resonant (PR) controller, represented by G_{PR_c} in Fig. 11. As the circulating currents also have a zero sequence component, it is also controlled (in addition to the $\alpha\beta$ component of the circulating current) using the PR controller. The model describing the circulating current behavior is given by (37) and

TABLE VI
SEMICONDUCTOR LOSSES AT DIFFERENT LOADING CONDITIONS

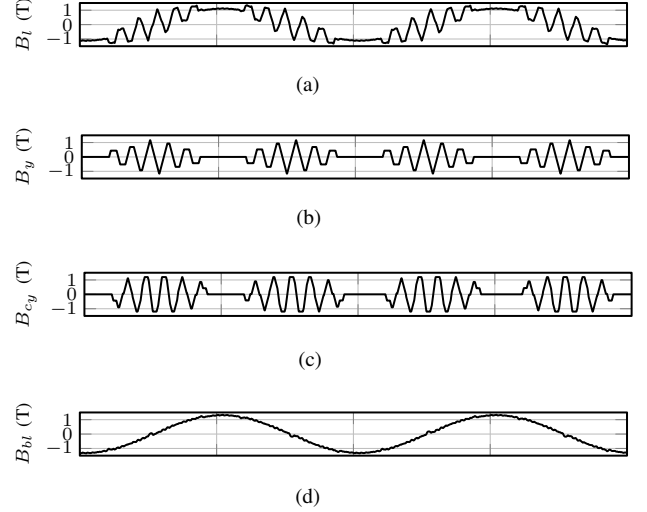| Load	0.25 pu	0.5 pu	0.75 pu	1 pu
Conduction losses (kW)	5.48	13.43	23.45	35.65
Switching losses (kW)	20.6	39.0	52.67	70.0
Total (kW)	26.08	52.43	76.12	105.65

(a)

(b)

(c)

(d)

Fig. 12. Simulation results at rated operating conditions. (a) Flux density in the limb of the cell of the integrated inductor, (b) Flux density in yoke of the cell, (c) Flux density in the common yoke, (d) Flux density in the bridge leg.

it is used to derive the controller gains, which are obtained as $k_{p_c} = 8.22 \ \Omega$ and $k_{i_c} = 4305 \ \Omega/s$.

B. Loss Evaluation

The semiconductor losses and the losses in the integrated inductor are evaluated in this section.

1) Semiconductor Losses: For the system specifications considered in this study, the VSCs can be realized using the 4.5 kV, 1200 A Insulated Gate Bipolar Transistor (IGBT). The use of the IGBT FZ1200R45KL3-B5 from the Infineon Technologies is considered. The losses are calculated using PLECS, where the required data are obtained from the device data sheet. The semiconductor losses at various loading conditions are given in Table VI.

TABLE VII
CORE AND COPPER LOSSES OF THE INTEGRATED INDUCTOR AT
DIFFERENT LOADING CONDITIONS

Load	0.25 pu	0.5 pu	0.75 pu	1 pu
Copper losses (kW)	1.03	2.85	5.89	10.17
Core losses (kW)	5.1	5.52	5.88	6.26
Total (kW)	6.13	8.37	11.77	16.43

TABLE VIII
VOLUMETRIC COMPARISON IN LTR.

Material	Amorphous	Laminated steel	Copper
Separate inductor	336	373	105
Integrated inductor	351	172	62
% change	+ 4.4%	- 53.8%	- 40.9%

2) Inductor Losses: The core and the copper losses of the integrated inductor are calculated for the high power system, with the design parameters specified in Table IV.

The Improved Generalized Steinmetz Equation (IGSE) [23] is used to calculate the core losses. The time domain simulation of the integrated inductor is carried out using the magnetic toolbox in PLECS, which uses permeance-capacitance analogy to model the inductor. The simulated flux density waveforms in various parts of the magnetic structure of the integrated inductor are shown in Fig. 12. The flux in the yoke has a major harmonic component at the carrier harmonic frequency, whereas the flux in the bridge legs has a dominant fundamental frequency component, as shown in Fig. 12(d). The flux in the limb is the addition of the common flux component and the circulating flux component, as shown in Fig. 12(a). The maximum value of the flux in the common yoke is the same as that of the top and the bottom yoke as shown in Fig. 12(b), which is in agreement with the analysis presented in section IV. Core losses due to these components are evaluated separately.

The copper loss is evaluated by considering the ac resistance of the winding, which takes into account the skin and proximity effects as outlined in [24]. The core and the copper losses of the integrated inductor at different loading conditions are calculated and given in Table VII.

C. Comparative Evaluation

The advantages offered by the integrated inductor is demonstrated by comparing its volume and losses with that of the separate inductor case. The values of the inductance, the flux density, the current density, and the window utilization factor are assumed to be the same in both the cases. Typically the Coupled Inductor (CI) is used to suppress the circulating current between the parallel VSCs and it is considered for circulating current suppression between the parallel VSCs in both the converter groups for the separate inductor case. Each of the converter groups are assumed to have separate line filter inductor with the value of $L_f/2$ and with the coil current of $I_x = I_{x_H} = -I_{x_L}$. Two limb magnetic structure is considered for the CI, whereas the line filter inductor is assumed to be realized using the three-phase three-limb inductor.

The line filter inductor is assumed to be made from the grain oriented laminated steel with lamination thickness of

TABLE IX
TOTAL CORE AND COPPER LOSSES FOR THE SEPARATE INDUCTORS
CASE AT DIFFERENT LOADING CONDITIONS

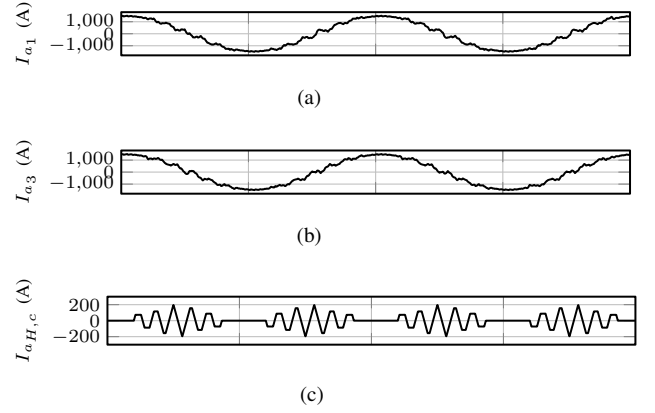| Load	0.25 pu	0.5 pu	0.75 pu	1 pu
Copper losses (kW)	1.55	4.64	9.81	17.04
Core losses (kW)	6.27	7.08	8.12	8.93
Total (kW)	7.82	11.72	17.93	25.97

Fig. 13. Simulation current waveforms. (a) Output current of VSC1 I_{a_1}, (b) Output current of VSC3 I_{a_3}, (c) Circulating current $I_{a_{H,c}}$.

0.35 mm, whereas the use of the amorphous alloys 2605SA1 is considered for the CIs. The volume of the various materials is compared and given in Table VIII. The integrated inductor leads to 26.2% reduction in the volume of the magnetic material and 40.9% reduction in the volume of the copper.

The core and the copper losses in the separate inductor case are evaluated and given in Table IX. As evident from Table VII and Table IX, the losses in the case of the integrated inductor are less compared to the separate inductor case over the whole operating range. This not only increases the system efficiency but also reduces the cooling requirement.

VI. SIMULATION AND EXPERIMENTAL RESULTS

Time-domain simulations are carried out using PLECS. Fig. 13 shows the simulated waveforms of the phase a at the rated load operation. The circulating current between the VSCs of the HSCG is shown in Fig. 13(c), which is within the defined limit. Only the current waveforms of the HSCG are shown as the waveforms of the LSCG are also identical ($I_{x_H} = -I_{x_L}$).

Fig. 14 shows the simulated current waveforms for a step response of the current control when the reference current was changed from 0.25 pu to 1 pu. The corresponding flux density waveforms for the phase a are also shown in Fig. 15. As it is evident for the Fig. 15(b), the dc component is avoided in the circulating flux due to the simultaneous sampling of the parallel VSCs [25]. As a result, the inductor saturation during the transient is avoided. The waveform of the output current of the HSCG has very small ripple component as shown in Fig. 14(b), which proves the effectiveness of the integrated inductor.

The experimental results were obtained for the system shown in Fig. 1. The electrical equivalent circuit of the
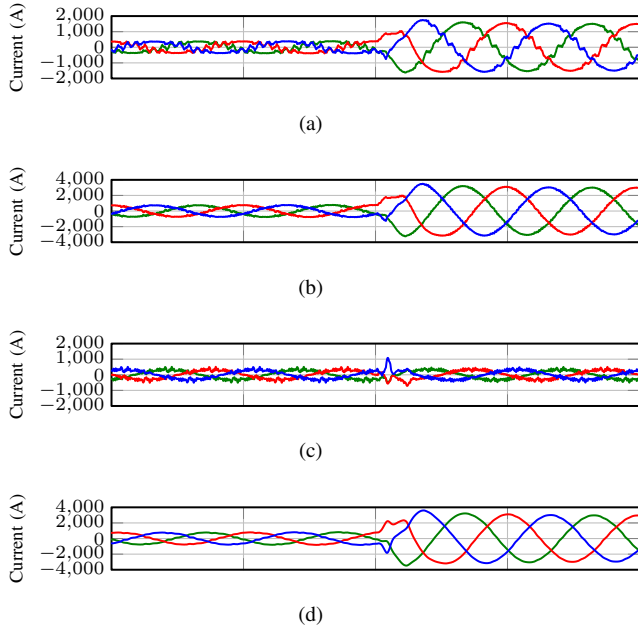
(a)

(b)

(c)

(d)

Fig. 14. Simulated waveforms for a step response of the current control when the reference current was changed from 0.25 pu to 1 pu. (a) Leg currents of all phases of VSC1 (I_{a_1}, I_{b_1}, I_{c_1}), (b) Resultant current of the high-side converter group (I_{a_H}, I_{b_H}, I_{c_H}), (c) Current through the shunt capacitive branch of the LCL filter, (d) Injected grid current ($I_{a,g}$, $I_{b,g}$, $I_{c,g}$).
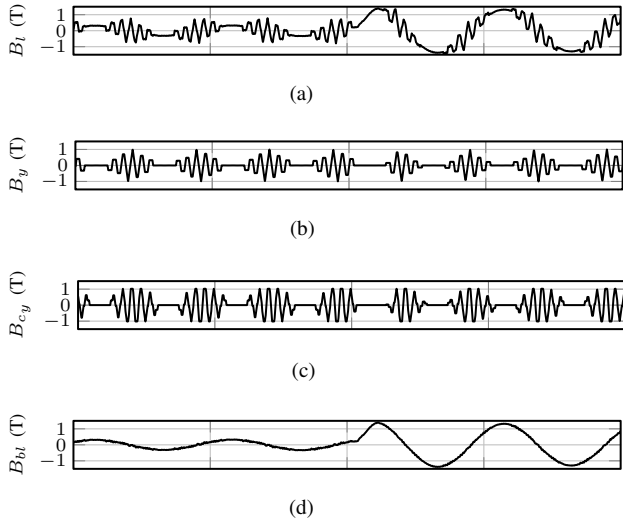

(a)

(b)

(c)

(d)

Fig. 15. Simulated flux density waveforms for a step response when the reference current was changed from 0.25 pu to 1 pu. (a) Flux density in the limb of the cell of the integrated inductor, (b) Flux density in yoke of the cell, (c) Flux density in the common yoke, (d) Flux density in the bridge leg.

integrated inductor along with the LCL filter arrangement is shown in Fig. 7. The VSCs of the HSCG and the LSCG are connected to separate dc-links, fed from two isolated dc supplies. The VSCs were modulated using the DPWM1 and the modulator is implemented using TMS320F28346 floating-point digital signal processor. The implemented inductor was built and its photograph is shown in Fig. 9(c). The dimensions of the implemented inductor are specified in Table IV. The
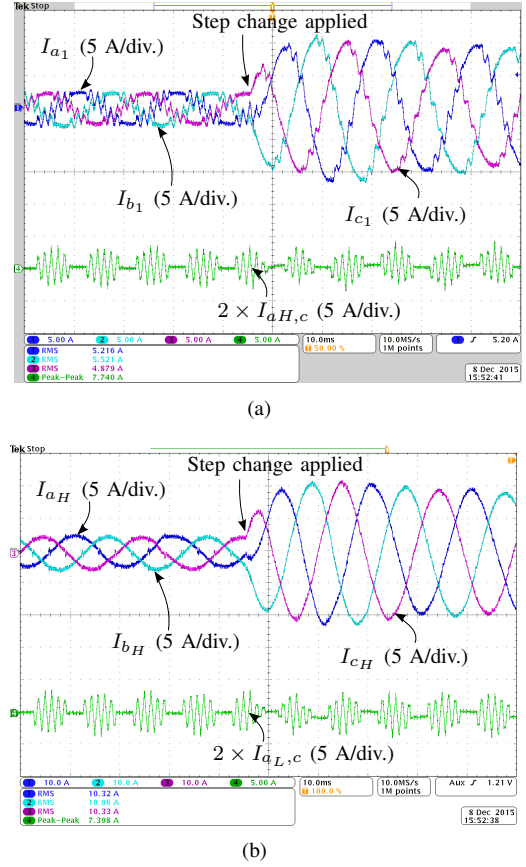

(a)

(b)

Fig. 16. Experimental waveforms for a step response when the reference current was changed from 0.25 pu to 1 pu. (a) Ch1: I_{a_1}, Ch2: I_{b_1}, Ch3: I_{c_1}, and Ch4: $I_{a_H,c}$, (b) Ch1: I_{a_H}, Ch2: I_{b_H}, Ch3: I_{c_H}, and Ch4: $I_{a_L,c}$.

cell structure is realized using amorphous alloys 2605SA1, whereas laminated steel is used for the bridge legs.

The integrated inductor offers inductance L_c to the circulating current and inductance L_f to the resultant line current. The LCL filter is used for the line current filtering, where L_f is used as a converter-side inductance of the LCL filter. The Y/Δ transformer is used with the star-side winding reconfigured as an open-ended winding. The leakage inductance of the transformer is measured to be 3.1 mH. The transformer leakage along with the discrete 1.9 mH inductor forms the grid-side inductor L_g. The damping branch R_d/C_d is used in parallel with the capacitive branch C_f to provide damping. The system parameters are specified in Table III.

The individual VSCs are operated with the switching frequency of 750 Hz, and the switched output voltages of the individual VSCs has a major harmonic component at the carrier frequency harmonics. However, these voltage components are phase shifted for two parallel interleaved VSCs and the integrated inductor offers very high inductance (L_c=39 mH) to these components. As a result, the circulating current between the VSCs of the HSCG $I_{a_H,c}$ is effectively suppressed, as shown in Fig. 16(a). The measured peak value of the circulating current between the VSCs of the HSCG is 1.6 A, which is around 15% of the amplitude of the rated output current of the individual VSCs. The circulating current between the VSCs of

the LSCG $I_{a_{L,c}}$ is also suppressed to 1.6 A (peak value), as shown in Fig. 16(b). In addition to the desired fundamental frequency component, the resultant current of the HSCG I_{a_H} also has ripple current components with the major harmonic frequency component at the $4th$ carrier harmonics, as shown in Fig. 16(b). The integrated inductor offers the desired line filter inductance (converter-side inductance of the LCL filter), as it is evident from the waveform quality of the resultant line current of the HSCG.

The experimental waveforms of Fig. 16 were captured when a step change (0.25 pu to 1 pu) is applied in the reference current. Fig. 16(a) shows the leg current of all the phases of the VCS_1, along with the circulating current between the VSCs of the HSCG $I_{a_H,c}$. The circulating current between the parallel converters of the LSCG is also shown in Fig. 16(b). The simultaneous sampling of the parallel VSCs avoids the dc flux injection during the transient conditions, as evident from the circulating currents $I_{a_H,c}$ and $I_{a_L,c}$. The circulating current controller also ensures the saturation free operation of the integrated inductor by controlling the fundamental frequency component in the circulating current to be zero.

VII. CONCLUSION

The current handling capability enhancement of the open-end transformer topology for the high power grid-connected applications is proposed. The converter-side winding of the transformer is configured as an open-ended and fed from the two converter groups. Each of the converter groups have two VSCs connected in parallel to achieve high current rating. The carrier signals of the VSCs are interleaved to improve the harmonic performance. The integrated inductor is also proposed, which suppresses the circulating current between the parallel interleaved VSCs and also offer the desired inductance for the line current filtering. The line filter inductors of both the HSCG and the LSCG are also integrated. As the common flux components of the HSCG and the LSCG are the same, they completely cancel each other. As a result, only four bridge legs are required compared to eight in the case of the separate inductors. The use of the integrated inductor leads to 26.2% reduction in the volume of the magnetic material and 40.9% reduction in the volume of the copper for the 12 MW, 3.3 kV WECS. The scheme to control the active and the reactive component of the injected current and the fundamental component of the circulating current in $I_{aH,c}$ and $I_{aL,c}$ is also proposed. The analysis is also supported by the simulations and the experimental results.

REFERENCES

[1] A. Nabae, I. Takahashi, and H. Akagi, "A new neutral-point-clamped PWM inverter," *IEEE Trans. Ind. Appl.*, vol. IA-17, no. 5, pp. 518–523, Sep. 1981.

[2] J. Rodriguez, S. Bernet, P. Steimer, and I. Lizama, "A survey on neutral-point-clamped inverters," *IEEE Trans. Ind. Electron.*, vol. 57, no. 7, pp. 2219–2230, Jul. 2010.

[3] T. Bruckner, S. Bernet, and P. Steimer, "Feedforward loss control of three-level active npc converters," *IEEE Trans. Ind. Appl.*, vol. 43, no. 6, pp. 1588–1596, Nov. 2007.

[4] F. Blaabjerg and K. Ma, "Future on power electronics for wind turbine systems," *IEEE J. Emerging Sel. Topics Power Electron.*, vol. 1, no. 3, pp. 139–152, Sep. 2013.

[5] G. Grandi, C. Rossi, D. Ostojic, and D. Casadei, "A new multilevel conversion structure for grid-connected pv applications," *IEEE Trans. Ind. Electron.*, vol. 56, no. 11, pp. 4416–4426, Nov. 2009.

[6] E. Levi, "Multiphase electric machines for variable-speed applications," *IEEE Trans. Ind. Appl.*, vol. 55, no. 5, pp. 1893–1909, May. 2008.

[7] K. Fujii, P. Koellensperger, and R. De Doncker, "Characterization and comparison of high blocking voltage IGBTs and IEGTs under hard- and soft-switching conditions," *IEEE Trans. Power Electron.*, vol. 23, no. 1, pp. 172–179, Jan. 2008.

[8] "Technical guidline: Generating plants connected to the medium-voltage network." BDEW Bundesverband der Energie- und Wasserwirtschaft e.V., [Online]. Available: http://www.bdew.de, Jun. 2008.

[9] S. K. T. Miller, T. Beechner, and J. Sun, "A comprehensive study of harmonic cancellation effects in interleaved three-phase vscs," *in Proc. IEEE Power Electronics Specialists Conference*, pp. 29–35, Jun. 2007.

[10] G. Gohil, L. Bede, R. Teodorescu, T. Kerekes, and F. Blaabjerg, "Line filter design of parallel interleaved vscs for high-power wind energy conversion systems," *IEEE Trans. Power Electron.*, vol. 30, no. 12, pp. 6775–6790, Dec. 2015.

[11] F. Ueda, K. Matsui, M. Asao, and K. Tsuboi, "Parallel-connections of pulsewidth modulated inverters using current sharing reactors," *IEEE Trans. Power Electron.*, vol. 10, no. 6, pp. 673–679, Nov. 1995.

[12] I. G. Park and S. I. Kim, "Modeling and analysis of multi-interphase transformers for connecting power converters in parallel," *in Proc. 28th Annual IEEE Power Electronics Specialists Conference*, vol. 2, pp. 1164–1170 vol.2, 1997.

[13] G. Gohil, L. Bede, R. Teodorescu, T. Kerekes, and F. Blaabjerg, "An integrated inductor for parallel interleaved three-phase voltage source converters," *IEEE Trans. Power Electron.*, vol. 31, no. 5, pp. 3400–3414, May. 2016.

[14] G. Gohil, L. Bede, R. Teodorescu, T. Kerekes, and F. Blaabjerg, "An integrated inductor for parallel interleaved vscs and pwm schemes for flux minimization," *IEEE Trans. Ind. Electron.*, vol. 62, no. 12, pp. 7534–7546, Dec. 2015.

[15] G. Gohil, L. Bede, R. Teodorescu, T. Kerekes, and F. Blaabjerg, "An integrated inductor for parallel interleaved vscs connected in a whiffletree configuration," *in Proc. IEEE Energy Conversion Congress and Exposition*, pp. 5952–5959, Sep. 2015.

[16] G. Gohil, L. Bede, R. Teodorescu, T. Kerekes, and F. Blaabjerg, "Magnetic integration for parallel interleaved vscs connected in a whiffletree configuration," *IEEE Trans. Power Electron.*, [Online early access], DOI: 10.1109/TPEL.2015.2514182, 2016.

[17] D. G. Holmes and T. A. Lipo, *Pulse Width Modulation for Power Converters: Principles and Practice*. Hoboken, NJ: Wiley-IEEE Press, 2003.

[18] A. Hava, R. Kerkman, and T. Lipo, "A high-performance generalized discontinuous PWM algorithm," *IEEE Trans. Ind. Appl.*, vol. 34, no. 5, pp. 1059–1071, 1998.

[19] G. Gohil, R. Maheshwari, L. Bede, T. Kerekes, R. Teodorescu, M. Liserre, and F. Blaabjerg, "Modified discontinuous pwm for size reduction of the circulating current filter in parallel interleaved converters," *IEEE Trans. Power Electron.*, vol. 30, no. 7, pp. 3457–3470, Jul. 2015.

[20] G. Gohil, L. Bede, R. Maheshwari, R. Teodorescu, T. Kerekes, and F. Blaabjerg, "Parallel interleaved VSCs: influence of the PWM scheme on the design of the coupled inductor," *in Proc. 40th Annual Conference on IEEE Industrial Electronics Society, IECON 2014*, pp. 1693–1699, Oct. 2014.

[21] A. Rockhill, M. Liserre, R. Teodorescu, and P. Rodriguez, "Grid-filter design for a multimegawatt medium-voltage voltage-source inverter," *IEEE Trans. Ind. Electron.*, vol. 58, no. 4, pp. 1205–1217, 2011.

[22] G. Gohil, L. Bede, R. Teodorescu, T. Kerekes, and F. Blaabjerg, "Design of the trap filter for the high power converters with parallel interleaved VSCs," *in Proc. 40th Annual Conference on IEEE Industrial Electronics Society, IECON 2014*, pp. 2030–2036, Oct. 2014.

[23] K. Venkatachalam, C. Sullivan, T. Abdallah, and H. Tacca, "Accurate prediction of ferrite core loss with nonsinusoidal waveforms using only steinmetz parameters," *in Proc. IEEE Workshop on Computers in Power Electronics*, Jun. 2002.

[24] P. Dowell, "Effects of eddy currents in transformer windings," *Proceedings of the Institution of Electrical Engineers*, vol. 113, no. 8, pp. 1387–1394, Aug. 1966.

[25] G. Gohil, L. Bede, R. Teodorescu, T. Kerekes, and F. Blaabjerg, "Integrated inductor for interleaved operation of two parallel three-phase voltage source converters," *in Proc. 17th European Conference on Power Electronics and Applications*, pp. 1–10, Sep. 2015.